Inclusion of spatial sampling and migration artefacts in AVO/Az analysis using Kirchhoff approximation

Hassan Khaniani and Daniel Trad

ABSTRACT

We quantify the uncertainty of linearized Amplitude Variation with Offset/Azimuth (AVO/Az) analysis of seismic P-P wave in a Horizontal Transverse Isotropic (HTI) model. We use Kirchhoff scattering and imaging operators to modify analytical values of AVO/Az based on the numerical artefacts produced by poor sampling and deficiencies of the operators to reproduce true amplitude migration. To compensate for errors due to numerical artefacts of sampling and migration, we present a multiparameter inversion for azimuthal parameters based on the reconstruction of total waveforms by representation on numerical dictionaries obtained by optimization. The computational operator for modeling the dictionaries is based on a 3D Kirchhoff scattering formulation, while the migration operator is based on Prestack Time Migration (PSTM). All operators consider the footprints of acquisition and migration operator in the estimation of AVO/Az characteristics of dictionaries. The amplitude and traveltime kernels during modeling are based on the linearized reflection coefficients of the HTI medium and the Double Square Root (DSR) equation of PSTM respectively. We show that the inclusion of the artifacts of acquisition and processing in the numerical estimation of AVO/Az values improves the accuracy of conventional analytical curve fitting. The Kirchhoff operator is a target oriented algorithm, which reduces the computation time of modeling and migration at specific target layers.

INTRODUCTION

Amplitude Variation with Offset/Azimuth (AVO/Az) analysis is a standard method for reservoir charecterization (Mallick & Frazer, 1991; Lynn et al., 1995; Rüger and Tsvankin, 1995; Rüger, 1997; 1998; Vavrycuk & Pšencík, 1998; Pšencík & Martins, 2001; Sayers and Dean, 2001; Chang & Gardner, 1993; Sayers & Rickett, 1997). Despite the widespread application of the method, the results are affected by insufficient spatial sampling of the data and inaccurate amplitudes obtained during migration. Removal of the spatial sampling footprints on the imaging result is a challenging task in seismic processing. The combination of the position of the source and receivers with several types of waves generates coherent noise which needs to be removed using notch filters in processing steps (Anstey, 1986 and Vermeer, 1990, Hampson, 1994 and 1995). Drummond et al. (2000) used a sequence of modeling and imaging to improve the Signal to Noise Ratio (SNR) as compared to the notch filtering approach. He predicted the patterns of acquisition noise by imaging of modeled data and substracted it from the migrated field data. Several studies show that interpolation of missing traces from incomplete data reduces the artefacts of spatial sampling in seismic imaging and AVO/Az analysis (Schonewille et al., 2003, Trad, 2009). Although, these processing steps can reduce the artefacts of spatial sampling, however, the deficiency of migration operator to estimate a true amplitude reflectivity function will still result in incorrectly estimated azimuthal properties. The goal of the true amplitude migration operator is to recover reflectivity functions that do not include the effects of the amplitude changes

such as geometrical spreading, transmition loss, etc. The inaccuracy of weight functions in diffraction stack integral and the numerical artefacts of migration (e.g., image bluring) also cause errors in estimation of reflectivity functions (Gray, 2013). The least squares deconvolution migration operators are known to be capable of reducing the artifacts such as image bluring and producing true amplitude reflectivity functions, but in practice, due to the higher computational cost in 3D acquisitions, least squares migration is not often implemented. In addition, similar to adjoint-based migrations algorithms, the accuracy of the result of least-squares migration depends to the input model parameters and weight functions.

In practice, the presence of numerical artefacts from acquisition and migration in AVO analysis are unavoidable (Zheng et. al., 2001). These numerical artefacts are stronger at longer offsets where the combination of migration diffraction stack integral and weight functions fails to produce a true amplitude image. To improve the accuracy of waveform inversion, statistical optimizations are appied to reduce the numerical artefacts and constrain the inversion results based on available prior knowledge of the medium (Tarantola and Valette, 1982; Tarantola, 1987; Duijndam, 1988a,b; Sen and Stoffa, 1995 Simmons and Backus, 1996; Buland and More 2003a, Buland and More 2003b, Russell et. al., 2003, Sen and Biswas, 2017). We use a different strategy from the previous studies in the sense that we modify the theoritical AVO/Az values to include the numerical artefacts. We show that the deviation of the numerical evaluaion of reflectivity functions from their analytical values create uncertainity for interpretation of an anisotroic medium.

Our model parameter inversion is similar to the prestack basis pursuit inversion that is based on representation of true waveform data by bases dictionaries multiplied by a scalar. The prestack basis pursuit inversion recovers the reflectivity functions (i.e., removes the source wavelet) using optimization of even and odd impulse pairs positioned at top and bottom of a layer boundary. The even pair has the same magnitude and sign, and the odd pair has the same magnitude, but opposite sign (Zhang et al., 2013). The approach is based on reconstruction of the signal by combination of even and odd pairs with the optimized multipliers. In this study, we reconstruct the waveform using the sensitivity components of AVO/Az and corresponding weight multipliers. We use Born scattering (e.g., Beylkin and Burridge, 1990) as the numerical approximation for estimation of reflectivity functions where the acquisition and processing parameters in modeling and migration are considered. We use the Kirchhoff approximation as a special case of the first order Born approximation in models which have a weak contrast in elastic properties across bedding interfaces. For approximation of the waveform characteristics in terms of traveltime and amplitude we use the Double Square Root (DSR) equation of Prestack Time Migration (PSTM) and the AVO/Az reflectivity functions. The method is applicable to different elastic models, such as orthorhombic and horizontally transverse isotropic, as well as various types of waves, such as PP reflections and PS conversions, etc. For this study, an HTI medium is considered, where we use the reflectivity function of Rüger (1997). The 2D approach of iterative waveform inversion using a PSTM operator and AVO scattering characteristics has been performed using both for isotropic acoustic and elastic approximation (Khaniani et al. 2012, Khaniani et al. 2014). Results of this study are focused on numerical aspects of one-step inversion which can be used in Kirchhoff based iterative inversion.

For the numerical examples, we compare different acquisition and model parameter scenarios for modeling and AVO/Az inversion. We show that due to the combination of different model parameters and different source-receiver configurations and migration, the

numerical AVO/Az reflectivities deviate from their analytical values. A pattern search algorithm is developed to construct the total waveform of modeled AVO/Az properties using several waveforms resulted from reflectivity function parameters. This algorithm forms a dictionary of basis functions for the target, then performs constrained least squares fitting search by combination of weight multiplier and the basis dictionary. We show that the solution of this approach is more stable compared to analytical curve fitting due to inclusion of numerical artifacts and the constraint of the solution by flexibility in the range of the multiplier.

This paper is organized as follow. First, we discuss a description of the amplitude and traveltime of Kirchhoff approximation in the context of the scattering formulation of an anisotropic medium. Second, we describe numerical problems associated with Kirchhoff modeling and migration for AVO/Az inversion. Third, we describe the basis dictionary formation and its application to AVO/Az fitting using synthetic and field data examples. Lastly, we discuss the advantage and limitation of the presented algorithm.

BORN SCATTERING IN ELASTIC MEDIUM

In this section, we present the mathematical basis for traveltime and amplitude of scattered waves of linear-elastic medium in the context of Born approximation. A known reference medium is perturbed with model parameters and the scattered wavefield is estimated using the first order Born approximation. True elastic parameters $c_{ijkl}(\vec{x})$, and the true density $\rho\ (\vec{x})$ are related to their corresponding reference model $c^0_{ijkl}(\vec{x})$ and $\rho^0(\vec{x})$ by,

$$c_{ijkl}(\vec{x}) = c^0_{ijkl}(\vec{x}) + \delta c_{ijkl}(\vec{x}), \qquad \rho(\vec{x}) = \rho^0(\vec{x}) + \delta\rho(\vec{x}), \tag{1}$$

where, $\delta c_{ijkl}(\vec{x})$ and $\delta\rho(\vec{x})$ are perturbation quantities for elastic parameters and density respectively. If we assume that $u_i = u_i(\vec{x},t)$ is a solution of the elasto-dynamic wave equation with a source function $f_i(\vec{x},t)$ calculated from the true model expressed by

$$\left(c_{ijkl}u_{k,l}\right)_{,j} + \rho\ddot{u}_i = -f_i, \quad i,j,k = 1,2,3 \tag{2}$$

then the perturbed wavefield $\delta\boldsymbol{u}_i(\vec{x},t)$ and the true wavefield $\boldsymbol{u}_i(\vec{x},t)$ are related to the solution of the reference medium $\boldsymbol{u}^0_i(\vec{x},t)$ by

$$u_i\ (\vec{x},t) = u^0_i(\vec{x},t) + \delta u_i\ (\vec{x},t). \tag{3}$$

For high frequency approximations, the single scattered wavefield components of the elastic waves can be expressed as (Beylkin and Burridge, 1990)

$$\delta u^{IR}_{jk} = -\partial_t^2 \int\left[\left(\left(\Delta\rho(\boldsymbol{x})\right)\delta_{ik} + \left(\Delta c_{ijkl}(\boldsymbol{x})\right)p^R_j p^I_l\right)h^I_k h^R_i\right]A^I_j A^R_k \delta(t-\phi^I-\phi^R)\mathrm{d}\boldsymbol{x}, \tag{4}$$

Where, ∂_t refers to the time derivative, the bracket terms describes the volume scattering potential $S^{IR}(x)$, superscripts I and R refer to incident and reflected waves, the subscripts jk indicate the displacement in the k-direction due to a point force in the j–direction. The terms A^I and A^R are true amplitude factors, ϕ^I and ϕ^R are the traveltimes

for the incident and reflected waves respectively. In addition, the operator Δ refers to the difference between the upper/lower media, the p is the slowness vector and h is the polarization unit vector. We can see that the radiation pattern in bracket varies with changes in density and stiffness tensor across the reflection boundary.

The models in this study correspond to the waves scattered from a smoothed interface that separates two elastic media. For such model, the volume scattering potential in equation (4) can be expressed by the surface integral Kirchhoff approximation, which is based on weak-contrast surface scattering (Beylkin and Burridge, 1990, Jaramillo and Bleistein, 1999, Shaw and Sen, 2004 and Kroode, 2012). In Figure 1, the amplitudes of scattered waves in a model with cracks are characterized by the isotropic plane and its normal (the axis of rotational symmetry). For the case of parallel vertical cracks, the vertical isotropic plane HTI model is considered. The seismic amplitudes in such a medium are affected by the phase angle of incidence between the direction of wave propagation and the symmetry axis. The HTI medium is described by (Musgrave, 1970 and Rüger, 2001)

$$C = \begin{pmatrix} c_{11} & c_{13} & c_{13} & 0 & 0 & 0 \\ c_{13} & c_{33} & c_{33}-2c_{44} & 0 & 0 & 0 \\ c_{13} & c_{33}-2c_{44} & c_{33} & 0 & 0 & 0 \\ 0 & 0 & 0 & c_{44} & 0 & 0 \\ 0 & 0 & 0 & 0 & c_{55} & 0 \\ 0 & 0 & 0 & 0 & 0 & c_{55} \end{pmatrix} \tag{5}$$

Generally, in an anisotropic medium, changes of c_{ijkl} and the angle/azimuthal dependent variations of p and h give additional terms to the reflectivity coefficients (Rüger, 2001 and Carcione , 2007) . Rüger (1997) linearized the exact solution of the Zoeppritz equation. The derivation is based on the continuity of stresses and displacements across the bedding interface that separates an upper HTI layer over a lower HTI layer. For a pre-critical angle of incidence in a weak contrast model, the change in c_{ijkl} and density ρ plays the main role in the scattering functions compared to the change in p and h. Shaw and Sen (2004) used the Born approximation in their equation for anisotropic scattering. They used slowness and polarization p and h of an isotropic background medium and obtain the same reflectivity coefficient as Rüger (1997).

Generally the weak-contrast linearized reflection coefficients $R(x)$ (Aki and Richards, 1980) and the scattering potential $S^{IR}(x)$ are related by (Moradi and Innanen, 2015) through the following equation,

$$R^{IR}(x) = -S^{IR}(x)\frac{\cos\theta^I}{2\cos\theta^R \sin(\theta^I + \theta^R)}, \tag{6}$$

where θ^I and θ^R are the angle of incident and reflected waves respectively. The linearized reflection coefficient as a function of phase and azimuth angles θ and φ for P-P mode is given by,

$$R_P^{HTI}(\theta,\varphi) = \sum_{k=1}^{6} \alpha_k \psi_k, \tag{7}$$

where the ψ_k are defined as

$$\psi_1 = \frac{\Delta v_P}{\bar{v}_p}, \psi_2 = \frac{\Delta Z}{\bar{Z}}, \psi_3 = \frac{\Delta G}{\bar{G}}, \psi_4 = \Delta\delta, \psi_5 = \Delta\varepsilon, \quad \text{and} \quad \psi_6 = \Delta\gamma. \tag{8}$$

The coefficients are defined by,

$$\alpha_1 = \frac{1}{2}tan^2\theta, \alpha_2 = \frac{1}{2}, \alpha_3 = -\frac{1}{2}\left(2\frac{\bar{v}_S}{\bar{v}_P}\right)^2 sin^2\theta, \alpha_4 = \frac{1}{2}\left(1+sin^2\varphi tan^2\theta\right)cos^2\varphi sin^2\theta,$$
$$\alpha_5 = \frac{1}{2}cos^4\varphi sin^2\theta tan^2\theta, \alpha_6 = \left(2\frac{\bar{v}_S}{\bar{v}_P}\right)^2 cos^2\varphi sin^2\theta, \tag{9}$$

where θ denotes the incident phase angle, $Z = \rho v_P$ is the P-wave impedance, ρ is the density and $G = \rho v_S^2$ is the shear wave modulus. Additionally, Δ denotes the difference between the properties across the bedding boundaries. The P-wave and S-wave velocities, v_P and v_S, and the anisotropic parameters are defined with the following relationships; $v_P = \sqrt{c_{33}/\rho}$, $v_S = \sqrt{c_{55}/\rho}$ and the Thomsen's parameters ε, δ and γ are defined by (Thomsen, 1986),

$$\delta = \frac{\left(c_{13}+c_{55}\right)^2 - \left(c_{33}-c_{55}\right)^2}{2c_{33}\left(c_{33}-c_{55}\right)}, \quad \varepsilon = \frac{c_{11}-c_{33}}{2c_{33}}, \quad \gamma = \frac{c_{44}-c_{55}}{2c_{55}}, \tag{10}$$

The traveltime of the scattering formulation in equation (4) is obtained using (Schneider, 1978, Claerbout, 1993),

$$t = \frac{r^I}{v^I} + \frac{r^R}{v^R} = \phi^I + \phi^R, \tag{11}$$

where, r^I is the length of the path of the incident wave from the source to the scatter point, and r^R is the length of the path of the reflected wave from the scatterpoint to the receiver. We use the Double Square Root (DSR) equation of PSTM for the estimation of total traveltime t. The v^I and v^R are the migration velocities of the incident and reflected waves, which are angle and azimuth dependant. Using the assumption of weak anisotropy, the phase velocity of a P-wave propagating in HTI can be linearized in terms of θ, φ, ε and δ (Tsvankin, 1997a and Tsvankin, 1997b)

$$v_P^{HTI}(\theta,\varphi) = v_{P0}\left[1+\varepsilon cos^4\varphi sin^4\varphi + \delta cos^2\varphi sin^2\theta\left(cos^2\theta + sin^2\varphi sin^2\theta\right)\right], \tag{12}$$

where v_{P0} is the P-wave velocity in isotropic media.

NUMERICAL MODELING AND MIGRATION

We consider a numerical model that consists of two flat layers, in which both upper and lower layers are transversely isotropic with the same axis of symmetry. A model with x- and y- lengths of $L_x = L_y = 3000$ m with the anisotropic parameters of Table 1 is created. The azimuth φ is referenced with respect to the x-axis direction, and the incident angle θ is estimated with respect to the target layer at a depth of 500 m and isotropic velocity $v_{P0} = 2500$ m/s. The receiver spacing in directions x and y are $dx_{rec} = dy_{rec} = 25$ m, and the subsurface bin size for modeling and migration is $dx_{bin} = dy_{bin} = 25$m. A Ricker wavelet with the dominant frequency of 17 Hz is used in the simulation.

We used equation (12) to estimate the variation of the P-wave velocity, for a model with a layer boundary at 500 m with $\delta = -0.1$ and $\varepsilon = -0.1$. As shown in Figure 2 the velocity variation is symmetric with respect to the anisotropic symmetry axis, where the maximum velocity is aligned with the azimuth of the direction of fractures (i.e., $\varphi = 90^o$) and is minimum in higher incident angles in the direction perpendicular to the fracture planes (i.e., $\varphi = 90^o$).

Due to the presence of HTI anisotropy, as shown Figure 2, the traveltimes for the scatter point diffractions are angle and azimuth dependent. Thus, for estimation of the traveltime of a diffraction of a single scatterpoint, the incident traveltime ϕ^I is estimated based on the velocity equation (12) with angle of incident θ^I and the azimuth of the source $\boldsymbol{x}_s$ to the scatterpoint position $\boldsymbol{x}$, while the reflected traveltime ϕ^R is estimated based the reflection angle θ^R and azimuth of the scatterpoint position $\boldsymbol{x}$ to the receivers $\boldsymbol{x}_g$. In scattering theory and also according to Huygens's principle, the superposition of all diffractions form the reflection curves. The diffraction curves that are not positioned on the reflection curve have negligible amplitude due to the destructive interference. This effect is complete for a large number of diffraction curves (i.e., smaller grid size) but it is incomplete on the boundaries of the model. Therefore, the Kirchhoff scattering modeling has artifacts on the boundaries, which can be minimized by increasing the model size. In Figure 2, different patterns of angle/azimuthal dependant diffraction traveltime from boundaries are shown by two white arrows. The arrows in Figure 2 are aligned with the direction of the axis of symmetry that indicate amplitude and traveltime of the HTI medium, while in Figure 2, they are on the fracture isotropic plane that indicates isotropic behaviour. In the modeling scheme, the reflectivity function is estimated based on the incident wave parameters, but the velocity variation is estimated based on incident and reflected waves for each source and receiver pair. In Figure 3, the variation of traveltime and amplitude of the reflection curve of the receivers is displayed on both x- and y- directions. Due to AVO/Az effects of HTI, both traveltime and amplitudes of reflection curves as well as the diffractions of side boundaries exhibit different patterns in the x- and y- direction. In the next section, in order to discuss the uncertainty of the AVO/Az inversion due to the footprints of migration and acquisitions, we use Kirchhoff modeling and corresponding PSTM imaging to map these variations from data domain into the model domain.

EFFECTS OF SAMPLING AND MIGRATION ON AVO INVERSION

Proper sampling of seismic waves in 3D field acquisitions is costly. For a single shot, sampling in the direction of the receiver lines (in-line) is generally satisfactory, while the sampling in the orthogonal direction (cross-line) is usually poor. In addition, sometimes due to practical obstacles such as rivers, lakes, land permissions, or cities, some sources and receivers are missing. This sampling deficiency makes it difficult to achieve true amplitude migration gathers, which are necessary in order to perform AVO/Az analysis. In fact, true amplitude migration gathers are difficult to achieve even with well sampled data. Least-squares migration could potentially alleviate this problem but is rarely used because of its cost. Calling G the modeling operator and G^T the migration operator, the obtained image through prestack migration (i.e., $\tilde{m} = G^T d$) is inaccurate because we have (e.g., Nemeth et al., 1999, Yu et al., 2006),

$$\mathrm{m} = (\mathrm{G}^T G)^{-1} \tilde{m}, \tag{13}$$

which affects the result of AVO/Az inversion. The acquisition sampling problem is related to the blurring operator $G^T G$ and typically has strong off-diagonal components when the data are incomplete. Another factor that affects the capability to achieve true amplitude image gathers is the design of the amplitude weights used in the operator itself. These weights have complex and costly expressions when theory is followed strictly. Instead, it is common to apply approximations to make these weights data independent, for example assuming constant velocity or very smooth variations. These approximations often affect AVO preservation as well, and that is not compensated by least squares migration.

To demonstrate sampling artifacts on numerical analysis, we perform the modeling and migration of the data obtained from isotropic and HTI scenarios. The isotropic scenario is obtained from the v_P , v_S and ρ of Table 1, and its analytical values of AVO are shown in Figure 4a. Figure 4b is obtained by a receiver sampling with $dx_{rec} = dy_{rec} = 25$ m. In this case, for a peak wavelet frequency of 17 Hz and the given velocity of the upper layer, the sampling is satisfactory for recovering of analytical AVO trends. In Figure 4b, the contour lines of iso-amplitude for numerical results show deviations from the trends of analytical AVO values. These deviations are more visible in the case of poor sampling shown in Figure 4c, where, we keep the in-line geophone spacing $dx_{rec} = 25$ but the cross-line is set to be $dy_{rec} = 375$ m. Although this model is an isotropic scenario, poor sampling causes deviations of AVO variations from the analytical values, which potentially increase the uncertainty of the inversion and can be misinterpreted as an anisotropic scenario.

We performed a similar analysis on an HTI anisotropic model with the isotropic and anisotropic parameters given in table 1. The horizontal axis of symmetry of the model is chosen to be $\varphi = 45^o$, where its analytical AVO/Az values are shown in Figure 5a. Similar to the dense sampling example of the isotropic scenario (i.e., $dx_{rec} = dy_{rec} = 25$ m), the anisotropic trends of AVO/Az in the numerical evaluation in Figure 5b are quite similar to the analytical values. The poor sampling example of $dx_{rec} = 25$ and $dy_{rec} = 375$ m shows distortion of the amplitude AVO/Az values as shown in Figure 5c. Because of the effects of poor sampling, the inline direction and the migration operator, the numerical AVO/Az results are not consistent with the expected analytical evaluations. Consequently, less

balanced migration amplitudes in short and far offsets increase the uncertainty of inversion and interpretation of anisotropic patterns.

The analytical radiation pattern of the model with parameters defined in Table 1 has amplitudes that decrease with offset in all azimuths (see Figure 4). As seen in Figure 5, for reflectivity functions with decreasing amplitude variation with offset, it is difficult to demonstrate the inability of the migration operator to recover the true amplitude of reflectivity for all offsets and azimuths. For this situation, the radiation pattern of numerical AVO/Az has a similar trend of decreasing amplitude with increasing offset that is expected in the analytical evaluation. In Figure 6 we demonstrate this problem using different input model parameters, as defined in Table 2. Compared to the model parameters of Table 1 only the relative contrasts of v_P and ρ are changed. The reference azimuth of the symmetry axis is $\varphi = 0$. Analytical evaluation of the reflectivity function shows increasing amplitude with offset in azimuth direction of $\varphi = 0^o$ and decreasing amplitude with offset in in the azimuth direction of $\varphi = 90^o$. The analytical AVO/Az values in Figure 6a are compared to values obtained from the well-sampled data in Figure 6b and a poorly-sampled data in Figure 6c. Even with well-sampled data, only small offset amplitudes of the numerical evaluation are consistent with the amplitudes of the analytical evaluation. For larger offsets, inadequate true amplitude migration produces errors in AVO/Az analysis. The errors of AVO/Az analysis are greater with the poor sampling scenario in Figure 6c. In Figure 7, we chose the amplitudes along OB, OC, OD, OE and OF direction (see Figure 6a) which represent the azimuth of 0°, 30°, 45°, 60° and 90° respectively. The values of extracted amplitudes in Figure 6a, b and c are plotted in Figure 7a, b, and c respectively. Deviations of numerical evaluation from the analytical values are due to deblurring effects of equation (13) and inaccuracy of the true amplitude migration operators.

BASIS DICTIONARY FITTING (BDF) ALGORITHM

To perform the inversion, we build a basis dictionary by taking the sensitivity of the column vectors for the reflectivity function $\boldsymbol{R}(\theta,\varphi)_{MN\times 1}$ to small model perturbation $\partial\psi_k$ in equation (7). These vectors are referred to as the Jacobian component of seismic response given by,

$$J_k = \frac{\partial \boldsymbol{R}(\theta,\varphi)}{\partial \psi_k}, \quad \mathrm{k} = 1, 2, \cdots, 6, \tag{14}$$

where, the Jacobian J generalizes the gradient of a scalar-valued function of multiple parameters in $\boldsymbol{R}$. We refer to J_k as the basis dictionary α_k in equation (9) with the footprints of acquisition and migration. For estimation of J for each model parameter, the contrast of that parameter is modeled by scattering, and migrated. For inversion of seismic data $\boldsymbol{d}(\theta,\varphi)_{MN\times 1}$, the relationship between basis dictionaries J_k and model parameter can be expressed as a linear problem,

$$\begin{bmatrix} d(\theta_1,\varphi_1) \\ d(\theta_1,\varphi_2) \\ \vdots \\ d(\theta_M,\varphi_N) \end{bmatrix}_{(MN)\times 1} = \begin{bmatrix} \alpha_1(\theta_1,\varphi_1) & \alpha_2(\theta_1,\varphi_1) & \cdots & \alpha_6(\theta_1,\varphi_1) \\ \alpha_1(\theta_1,\varphi_2) & \alpha_2(\theta_1,\varphi_2) & \cdots & \alpha_6(\theta_1,\varphi_2) \\ \vdots & \vdots & \vdots & \vdots \\ \alpha_1(\theta_M,\varphi_N) & \alpha_2(\theta_M,\varphi_N) & \cdots & \alpha_6(\theta_M,\varphi_N) \end{bmatrix}_{MN\times 6} \begin{bmatrix} \psi_1 \\ \psi_2 \\ \vdots \\ \psi_6 \end{bmatrix}_{6\times 1}, \tag{15}$$

where, M and N are the total number of incident phase angles and azimuths of the data respectively. In equation (15), these dictionaries are the basis for AVO/Az curve fitting techniques which are valid for small angle of incidence and weak-contrast models. The linear problem in (15) is often solved in the context of l_2 norm optimization. The l_2 – norm optimization is sensitive to outlier noise which may give errors in AVO/Az inversion. In addition, the pattern of the isotropic dictionary for ψ_1 is similar to ψ_3 which makes it difficult to recover the v_P and ρ. Similarly, positive and negative amplitudes variations of anisotropic dictionaries ψ_4, ψ_5 and ψ_6 tend to cancel one another, increasing the errors of inverted values for ε , γ and δ.

In this study, as shown in Figure 8, we implement a direct pattern search algorithm that is based on a constrained bounded least-squares problem. For each perturbed model a linear fitting objective function is minimized according to,

$$S = \left\| G^T d - F \right\|_2 + \eta \left\| 1 - ncorr\left(G^T d, F\right) \right\|_1, \tag{16}$$

where, F is define as

$$F = \left(\sum_{\lambda=1}^{N_k} \sum_{k=1}^{6} w_{\lambda k} G^T G\left(\psi_k\right) \right), \tag{17}$$

where, the weights multiplier $w_{\lambda k}$ with the subscripts λ varies from 1 to the number of weight coefficients for fitting N_k . The regularization term η and normalized cross correlation operator $ncorr$ ensure that the radiation pattern of the constructed waveform has a shape similar to the pattern of the field data. This algorithm constructs the migration result by a combination of basis dictionary functions and multipliers.

The numerical dictionaries are formed with the same migration operator G^T and stored on disk. The elements of the stored dictionaries are multiplied by the weight functions $w_{\lambda k}$ (i.e., $w_{\lambda k} G^T \mathrm{G}(\psi_k)$). To perform the inversion of the model parameters, the dictionaries of all perturbations are combined and compared with their corresponding values in true data. The best solution is chosen by the least squares fit with highest correlation.

Figure 9 shows an example of an analytical dictionary with six basis functions estimated without the footprint of acquisition and migration. Figure 10 illustrates a different numerical dictionary with six-basis functions, this time using the acquisition parameters, i.e., position of sources and receivers and patch geometry. Here, similar to the true data acquisition, the receiver configuration overlaid in Figure 10 is used and the migration bin size is chosen to be 25 x 25 m, with a wavelet of 17 Hz and $\Delta t = 2$ ms. The model is 3000 x 3000 m with a maximum recording time of $t_{\max} = 1.5$ s. Although, the trend of analytical values has a similar pattern to the numerical evaluation, the distortion of amplitude due to the poor receiver sampling is visible at larger offsets. For the models where analytical

amplitudes increase with offset, with a migration operator inadequate for true amplitude reflectivity compensation, the result of numerical evaluation may produce a trend inconsistent with the analytical evaluation. Consequently, due to inclusion of the acquisition and migration footprints in the construction of the numerical dictionary, the result of inversion obtained from numerical dictionary is more accurate compared to the result obtained from the analytical dictionary. The accuracy of inversion using numerical AVO/Az basis dictionaries depends on the accuracy of the initial model, different types of wave superposition and the processing steps. For modeling G and migration operator G^T, the initial velocity model and anisotropic parameters of each scatterpoint are obtained from the properties of upper layers, which ensures that the same traveltime is considered for all basis dictionaries.

For estimation of the unknown azimuths of the symmetry axis, we perform modeling for each reference axis of symmetry and compare the traveltime and amplitude of modeled data with the corresponding values in true data. This approach is computationally expensive, since it requires forward modeling and migration operations for each symmetry axis azimuth. To reduce the computational costs, the time slice of a reference azimuth of symmetry axis is spatially rotated with respect to the position of the scatterpoint and compared with corresponding values in true data. The six-basis dictionary is combined with the weights $w_{\lambda k}$ and the inversion result is obtained by minimizing the misfit S. In this approach, the solution of such a problem is not necessarily unique, but by constraining the limits of $w_{\lambda k}$ the solution can approach the values of true parameters. In addition, we use a regularization term to maximize the similarity of the constructed waveform with that of the true data to find the best solution. For a quantitative comparison, the residual norms of the inversion by both analytical and numerical basis dictionaries are compared in Figure 11. The residual norm obtained from the numerical dictionary is smaller than the one obtained from analytical inversion. Although the inversion is performed on the synthetic data and the solution is constrained for this experiment, the residual norm of the proposed approach gives a correlation of 0.99, higher than the correlation of 0.98 achieved from the analytical basis dictionary. Hence, using the proposed approach we can reduce the uncertainty of the inversion due to numerical artifacts of acquisition and migration.

FIELD DATA EXAMPLE

In this section, we perform the AVO/Az analysis on a field data set. A Common Image Gather (CIG) obtained from the acquisition fold of 221 is provided by an oil operating company. The main processing steps were static corrections, air blast compensation, inline and crossline azimuthal low frequency attenuation, velocity analysis and PSTM. In this experience, it was hard to find the anisotropic radiation pattern in field data due to small values of anisotropic parameters. We had to rely on petrophysical descriptions for alignment of fractures and their parameters. In Figure 12a, we show a time slice of a formation at the depth of 3200 m, then used interpolation to map trace amplitudes into x-y coordinates. In Figure 12b, we tried the BDF algorithm with initial anisotropic values of $\varepsilon = -.05$, $\delta = -0.01$ and $\gamma = 0.1$ for the upper layer. The AVO/Az pattern obtained from BDF algorithm shows consistency of construction of radiation patterns of the field data CIG gather.

DISCUSSIONS

The inversion strategy based on the basis dictionary reduced the uncertainty caused by acquisition limitations and migration inaccuracies by including their resulting numerical artifacts into the basis functions. The approach is based on the PSTM and corresponding forward modeling, which requires less computation time as compared with the PSDM approaches. The PSTM is accurate for models with smooth velocity variation. For models with higher complexity, computation of traveltime has to be done more accurately by ray tracing. We assume that the data contain only primary pre-critical P-to-P reflection waves (i.e., multiples free) and the subsurface structures are not complex. The effects of interference of primary waves with other types of waves and structural complexity of the model can be modeled by finite element or finite difference algorithms. For modeling and imaging operators of 3D models with strong lateral variation in elastic properties ray tracing can be used for accurate modeling and migration.

The model provided in this study is based on the assumption of weak-contrast reflectivity with two transversely isotropic layers with the same axis of symmetry. The solution of such a problem is more accurate for small angles of incident up to the critical angles (e.g., 40 degrees). For solution of more complicated model, the numerical finite difference time domain schemes provide more accurate approximation for forward modeling.

For computational efficiency, in our numerical examples we assumed that the azimuthal distribution of anisotropic parameters in the HTI medium for a single shot record is the same as the CIGs from all shot records. Here, we perform a numerical experiment to demonstrate that our approximation is reasonable. In Figure 13a, a single shot record positioned at $(x, y) = (0, 0)$ m of a model having fracture plane with axis of symmetry $\varphi = 45^o$ and maximum angle of incident of $\theta = 45^o$, is migrated using a PSTM operator. The receivers cover the entire model with $dx_{rec} = dy_{rec} = 50$ m. The migration velocity for traveltime computation is the same velocity used in modeling operator. The radiation pattern obtained from the migrated result is symmetric around the azimuth of symmetry axis, which is consistent with the analytical evaluation of an HTI medium. We used 441 shot records to simulate the CIG gathers in an HTI medium. The dotted box in Figure 13b represents the acquisition region where the shot records are simulated. The source spacing in x and y direction is 50 m. The result of stacking of all migrated shots in Figure 13c shows that the amplitude of the time slice is balanced in all directions, which restricts the estimation of the axis of symmetry from post stack results. Since the model properties are the same in all parts of the model, the simulated CIG gathers show similar trends of symmetry axis as seen in the shot records. For example, the PSTM gather 'A' in Figure 13d is formed at the position of the center of the model within the aperture with maximum angle of incident of 45º. In Figure 13d, the gathers B, C and D are overlain in a single image for comparison. Despite different acquisition fold of each gather, the radiation patterns of all gathers are consistent with the analytical evaluations. In this study we used a single shot migration to represent the CIG gathers, but in practical applications similar to

the analysis of Figure 13, the combination of different geometries of sources, receivers and model parameters should be taken into account for simulation of CIG gathers.

CONCLUSIONS

We developed a numerical work flow to modify the analytical AVO/Az values for multiparameter inversion of pre-critical reflection data. We applied a Kirchhoff forward modeling and migration algorithm to include the numerical artifacts of sampling and deficiencies of migration in AVO/Az waveform inversion. The approach is based on generation of numerical basis functions compiled into a dictionary and the identification of their patterns in the data through an optimization algorithm to identify isotropic and azimuthal anisotropic parameters in data. The numerical basis dictionary reduces the errors of AVO/Az analysis compared to a standard curve-fitting of analytical values as often performed. To reduce the computational cost of inversion in 3D models, the linearized solution of the seismic reflection inverse problem is solved using standard PSTM and corresponding forward modeling. The AVO/Az approximation of weak contrast anisotropic models and Double Square Root (DSR) equation for traveltime consideration of P-to-P are implemented during inversion. The procedure is analytically and numerically compared with the expected amplitudes of different acquisition patterns of 3D anisotropic media. In this technique, we relate the gradient function to the sensitivity of radiation pattern of scatterpoints to subsurface isotropic and anisotropic parameters. The approach is different from analytical curve-fitting since they are based on improving SNR on the field data but, here, the same artefacts exist in both data and numerical AVO/Az values. As a future study, the current algorithm may be implemented for analysis of reflectivity functions of P-to-P and P-to-S waves in other types of model such as VTI and orthorhombic.

ACKNOWLEDGMENT

The authors acknowledge the support from sponsors of CREWES and NSERC (Natural Science and Engineering Research Council of Canada) through the grant CRDPJ 461179-13. Thanks to Shahpoor Moradi and David Henley for helpful discussions and suggestions.

REFERENCES

Aki, K., and Richards, P. G., 1980, Quantitative Seismology: Theory and Methods, W.H. Freeman and Company.

Anstey, N. A., 1986, Whatever happened to ground roll?: The Leading Edge, 5(3), 40-45.

Beylkin G., and Burridge R., 1990, Linearized inverse scattering problems in acoustics and elasticity, Wave Motion, 12, 15–52.

Bleistein, N. (1987). On the imaging of reflectors in the earth. Geophysics, 52(7), 931–942.

Buland, A. and Omre, H, 2003a, Bayesian linearized AVO inversion: Geophysics, 68, 185-198.

Buland, A. and Omre, H, 2003b,, Joint AVO inversion, wavelet estimation and noise-level estimation using a spatially coupled hierarchical Bayesian model: Geophysical Prospecting, 51: 531–550.

Carcione, J. M., 2007, Wave fields in real media: wave propagation in anisotropic, anelastic, porous, and electromagnetic media, 2nd ed: Elsevier, Amsterdam.

Chang C.H. and Gardner G.H.F. 1993, Effects of vertically aligned fractures on reflection amplitudes: an amplitude-versus-offset study: SEG meeting, Expanded Abstracts.

Drummond, J. M., Budd, A. J. L., Ryan, J.W., 2000, Adapting to noisy 3D data – attenuating the acquisition footprint: SEG meeting, Expanded Abstracts.

Duijndam, A.J.W., 1988a. Bayesian estimation in seismic inversion. Part I: Principles, Geophys. Prospect.,: 36, 878-898.

Duijndam, A.J.W., 1986b. Bayesian estimation in seismic inversion. Part 11: Uncertainty analysis, Geophys. Prospect.,: 36, 899-918.

Gray S. H., 2013, Spatial sampling, migration aliasing, and migrated amplitudes: Geophysics, 78, no. 3, S157–S164.

Grésillaud, A. and Cara, M. 1996, Anisotropy and P-wave tomography: a new approach for inverting teleseismic data from a dense array of stations: Geophysical Journal International, 126: 77–91.

Hampson, G., 1994, Relationships between wavefield sampling and coherent noise attenuation: Presented at the 56th EAEG Conference and Technical Exhibition.

Hampson G., 1995, The relationship between wavefield sampling and coherent noise attenuation in the CMP method: SEG meeting, Expanded Abstracts.

Jaramillo, H. and Bleistein, N., 1999, The link of Kirchhoff migration and demigration to Kirchhoff and Born modeling: Geophysics, 64(6), 1793–1805.

Khaniani H., Bancroft J. C., and Margrave G. F., 2012, Full waveform inversion algorithm using Common Scatter Point (CSP) gathers: SEG meeting, Expanded Abstracts.

Khaniani, H., Bancroft, J. C., and Lunen v. E., 2016. Iterative multiparameter waveform inversion of precritical reflection data using prestack time Kirchhoff approximation: Geophysics, 81, R15-R27.

Kroode T. F., 2012: A wave-equation-based Kirchhoff operator: Inverse Problems, 28(11), 115013.

Lynn H. B., Simon K. M., Layman M., Schneider R., Bates C.R. and Jones M. 1995. Use of anisotropy in P-wave and S-wave data for fracture characterization in a naturally fractured gas reservoir: The Leading Edge, 14, 887-893.

Mallick S., and Frazer L. N., 1991, Reflection/transmission coefficients and azimuthal anisotropy in marine seismic studies: Geophysical Journal International, 105, 241-252.

Moradi, S. and Innanen K. A., 2015. Scattering of homogeneous and inhomogeneous seismic waves in low-loss viscoelastic media: Geophysical Journal International, 202, 1722-1732.

Musgrave, M. J. P., 1970, Crystal acoustic: Holden Day.

Pšencík, I., and J. L. Martins, 2001, Properties of weak contrast PP reflection/transmission coefficients for weakly anisotropic elastic media: Studia Geophysica et Geodaetica, 45(2), 176–199.

Russell, B.H., Lines, L.R., and Hampson, D.P., 2003, Application of the radial basis function neural network to the prediction of log properties from seismic data: Exploration Geophysics 34, 15-23.

Rüger, A., and Tsvankin I., 1995, Azimuthal variation of AVO response for fractured reservoirs: SEG meeting, Expanded Abstracts, 1103–1106.

Rüger, A., and Tsvankin I., 1997, Using AVO for fracture detection: Analytic basis and practical solutions: The Leading Edge, v. 16/10, p.1429–1434.
Rüger, A., 1997, P-wave reflection coefficients for transversely isotropic media with vertical and horizontal axis of symmetry: Geophysics, 62, 713-722.
Rüger, A., 1998, Variation of P-wave reflectivity with offset and azimuth in anisotropic media: Geophysics 63, 935-947.
Rüger, A., 2001, Reflection coefficients and azimuthal avo analysis in anisotropic media: Geophysical Monograph Series.
Sayers, C.M. and J.E. Rickett, 1997, Azimuthal variation in AVO response for fractured gas sands: Geophysical Prospecting, 45, 165-182.
Sayers, C.M. and S. Dean, 2001, Azimuth-dependent AVO in reservoirs containing non-orthogonal fracture sets: Geophysical Prospecting, 49, 100-106.
Sen M. K., and Biswas R., 2017, Trans dimensional seismic inversion using the reversible jump Hamiltonian monte Carlo
Algorithm: Geophysics, 82(3):119–134.
Sen, M. K., and Stoffa P. L., 1995, Global Optimization Methods in Geophysical Inversion: Elsevier Science B. V., Amsterdam, The Netherlands.
Shaw, R. K., and M. K. Sen, 2004, Born integral, stationary phase, and linearized reflection coefficients in anisotropic media: Geophysical Journal International, 158, 225–238.
Schneider, W., 1978, Integral formulation for migration: Geophysics, 43, 49-76.
Schonewille, M. A., Romijn, R., Duijndam, A. J. W., and Ongkiehong, L., 2003, A general reconstruction scheme for dominant azimuth 3D seismic data: Geophysics, 68, 2092–2105.
Simmons, J. L. and Backus, M.M., 1996, Waveform-based AVO inversion and AVO prediction-error: Geophysics, 61, 1575-1588.
Tarantola, A., 1987, Inverse problem theory: Elsevier, Amsterdam.
Tarantola, A., and B. Valette, 1982, Inverse problems: Quest of information: Journal of Geophysics, 50, p. 159–170.
Trad D., 2009, Five-dimensional interpolation: Recovering from acquisition constraints: Geophysics, 74, no. 6, V123–V132.
Tsvankin, I., 1997a, Anisotropic parameters and P-wave velocity for orthorhombic media: Geophysics, 62, 1292–1309.
Tsvankin, I., 1997b, Reflection moveout and parameter estimation for horizontal transverse isotropy: Geophysics, 62, 614–629.
Thomsen, L., 1986, Weak elastic anisotropy: Geophysics, 51, 1954-1966.
Vermeer, G. J. 0., 1990, Seismic wavefield sampling: Processing the Recorded Wavefield, Geophysical references 5: Society of Exploration Geophysicists.
Vavrycuk V. and Pšencík I. 1998, PP-wave reflection in weakly anisotropic elastic media: Geophysics 63, 2129-2141.
Zhang R., Sen M. K., and Srinivasan S., 2013, A prestack basis pursuit seismic inversion: Geophysics, 78.
Zheng, Y., Gray, S., Cheadle, S., & Anderson, P., 2001, Factors Affecting AVO Analysis of Prestack Migrated Gathers :SEG meeting, Expanded Abstracts.

TABLE PAGES

Table 1: Model parameters used for evaluation of AVO/Az reflection coefficient for scenario I.

Two layer Model	v_P m/s	v_S m/s	ρ kg/m^3	$\delta^{(V)}$	$\varepsilon^{(V)}$	γ
Layer 1	2500	1627	2000	-0.1	-0.1	0.15
Layer 2	2700	1750	2120	-0.2	-0.2	0.30

Table 2: Model parameters used for evaluation of AVO/Az reflection coefficient for scenario II.

Modeling	v_P m/s	v_S m/s	ρ kg/m^3	$\delta^{(V)}$	$\varepsilon^{(V)}$	γ	φ^o
1	2300	1627	1880	-0.1	-0.1	0.15	0
2	2500	1750	2000	-0.2	-0.2	0.30	0

FIGURE PAGES

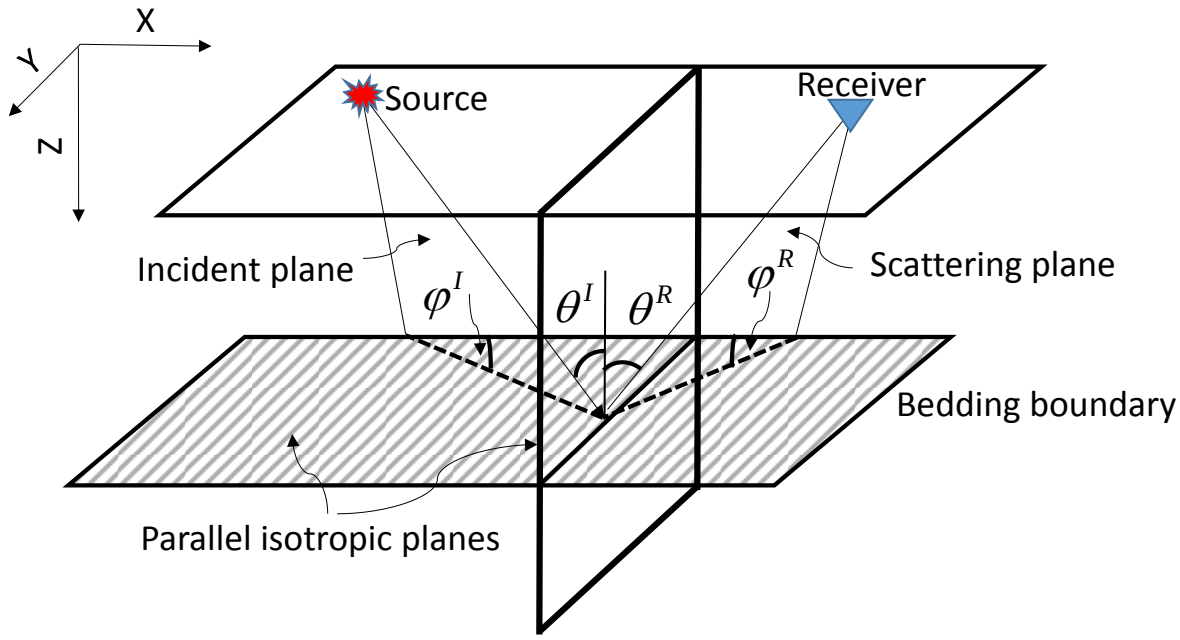

Figure 1: Schematic representation of reflection in transversely isotropic medium. A ray in the incident plane hits the scatterpoint on the bedding interface and scatters in all directions. The parallel isotropic planes characterizes the fracture orientation in HTI medium, where their elastic properties changes across bedding interface. At the specular phase angle θ and azimuth φ, the amplitudes of the scattered waves are singular with maximum amplitudes, which makes the reflection data.

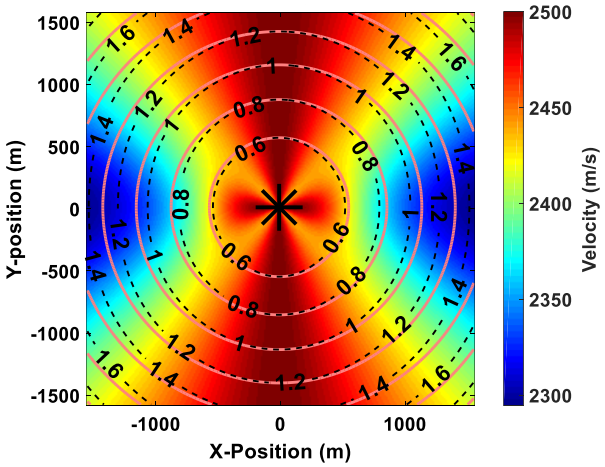

Figure 2: P-wave velocity variation for a HTI medium. The evaluation is based on a target layer at 500 m depth and an anisotropic medium with $\varepsilon = -0.1$, $\delta = -0.1$ and the isotropic velocity $v_{P0} = 2500$ m/s.

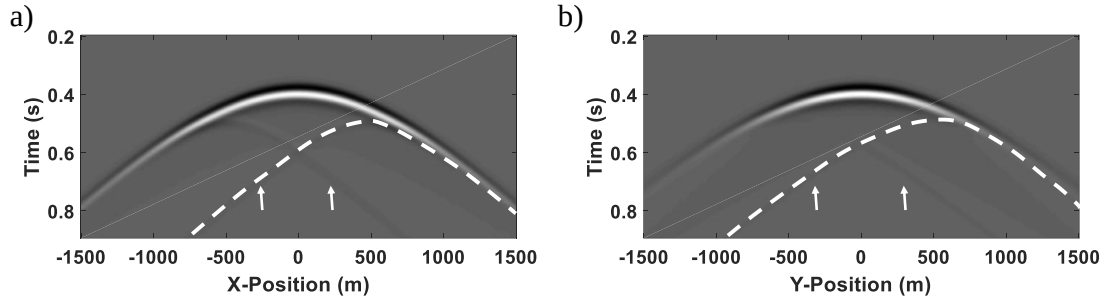

Figure 3: 3D modeled data obtained from a two-layer model with the parameters in Table 1, where the source is positioned at $\boldsymbol{x}_s = (0,0)$ and the effects of anisotropy are minimal in the direction of the isotropic plane at $\varphi = 90^o$. The receivers in a) are positioned aligned with the x- axis (i.e. $\varphi = 0^o, y = 0$) where the effects of anisotropic are greater (i.e., $\varphi = 0^o$) compared to b) where the receivers are positioned aligned with the $y-$ axis (i.e. $\varphi = 90^o, x = 0$).

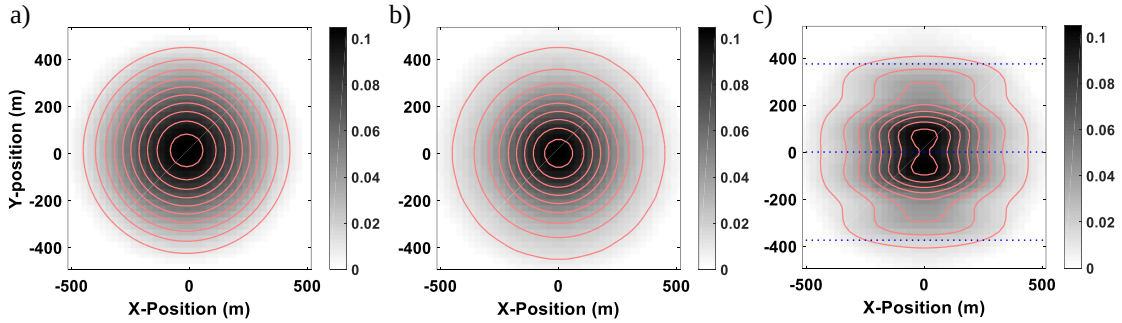

Figure 4: Evaluation of the radiation pattern for isotropic model in surface acquisition. a) Analytical evaluation of AVO values. The time slice of 0.4 s of migration amplitude for b) the well-sampled Kirchhoff modeled data and c) the poorly-sampled data. The receiver spacing in (b) is $dx_{rec} = dy_{rec} = 25\,\text{m}$ and the dotted line in (c) represents three receiver lines with $dx_{rec} = 25$ and $dy_{rec} = 375\,\text{m}$.

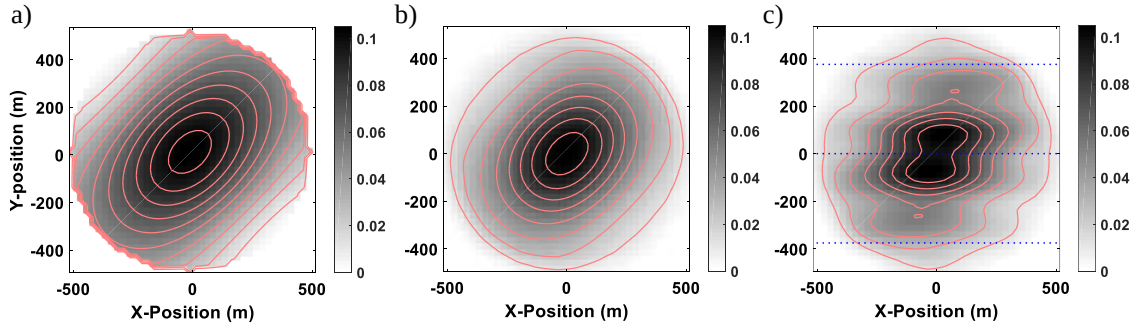

Figure 5: Evaluation of radiation pattern of anisotropic HTI model. a) Analytical evaluation of AVO/Az values for a HTI model with azimuth of axis of symmetry of $\varphi = 45^o$. The time slice of 0.4 s of migration amplitude for b) the well- sampled Kirchhoff modeled data and c) the poorly-sampled data. The receiver spacing in (b) is $dx_{rec} = dy_{rec} = 25\,\text{m}$ and the dotted line in (c) represents three receiver lines with $dx_{rec} = 25$ and $dy_{rec} = 375\,\text{m}$.

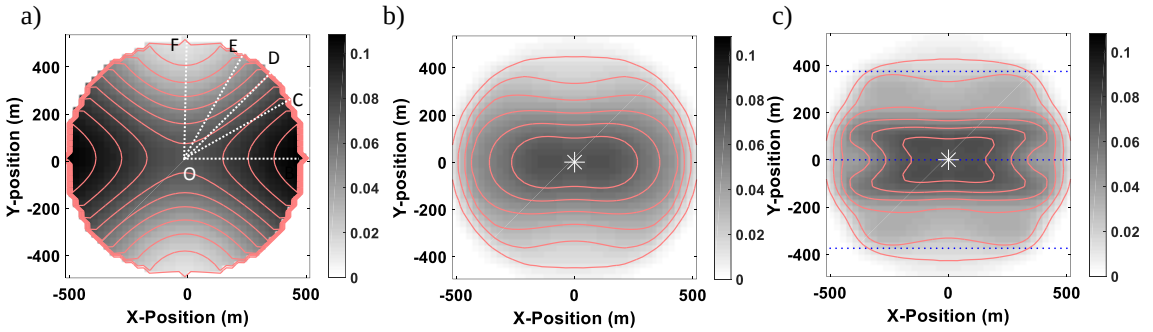

Figure 6: Evaluation of radiation patterns for an anisotropic HTI model. a) Analytical evaluation of AVO/Az values for a HTI model with azimuth of axis of symmetry of $\varphi = 0^o$. The time slice of 0.43 s of migration amplitude for b) the well-sampled Kirchhoff modeled data and c) the poorly-sampled modeled data. The receiver spacing in (b) is $dx_{rec} = dy_{rec} = 25$ m and the dotted line in (c) represents three receiver lines with $dx_{rec} = 25$ and $dy_{rec} = 375$ m.

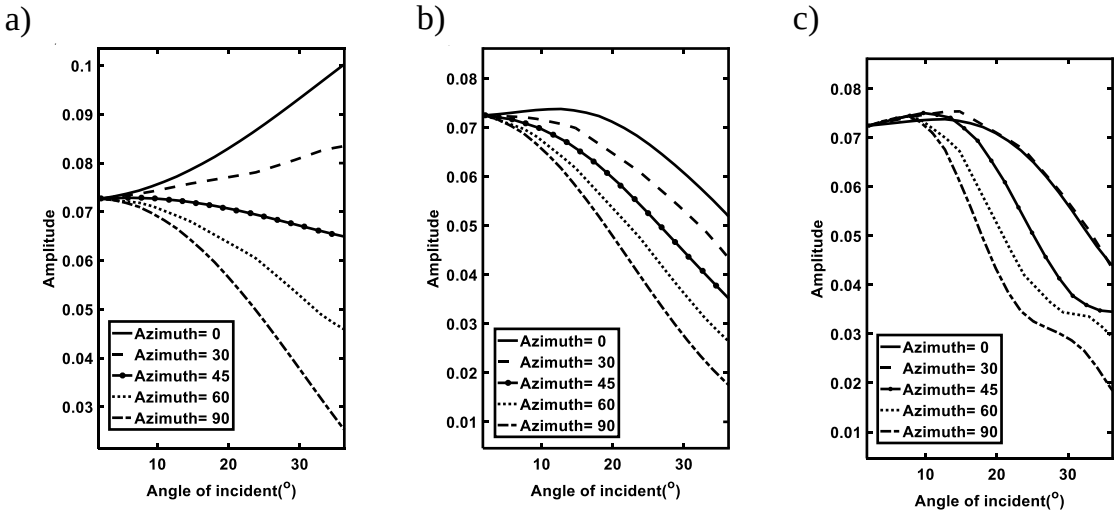

Figure 7: The values along OB, OC, OD, OE and OF directions in Figure 6 are extracted to represent the azimuth of 0º, 30º, 45º , 60º and 90º respectively. Due to artifacts of acquisition and migration, the corresponding values in the analytical evaluations in panel a) deviate from numerical evaluation in b) well-sampled and c) poorly-sampled scenarios.

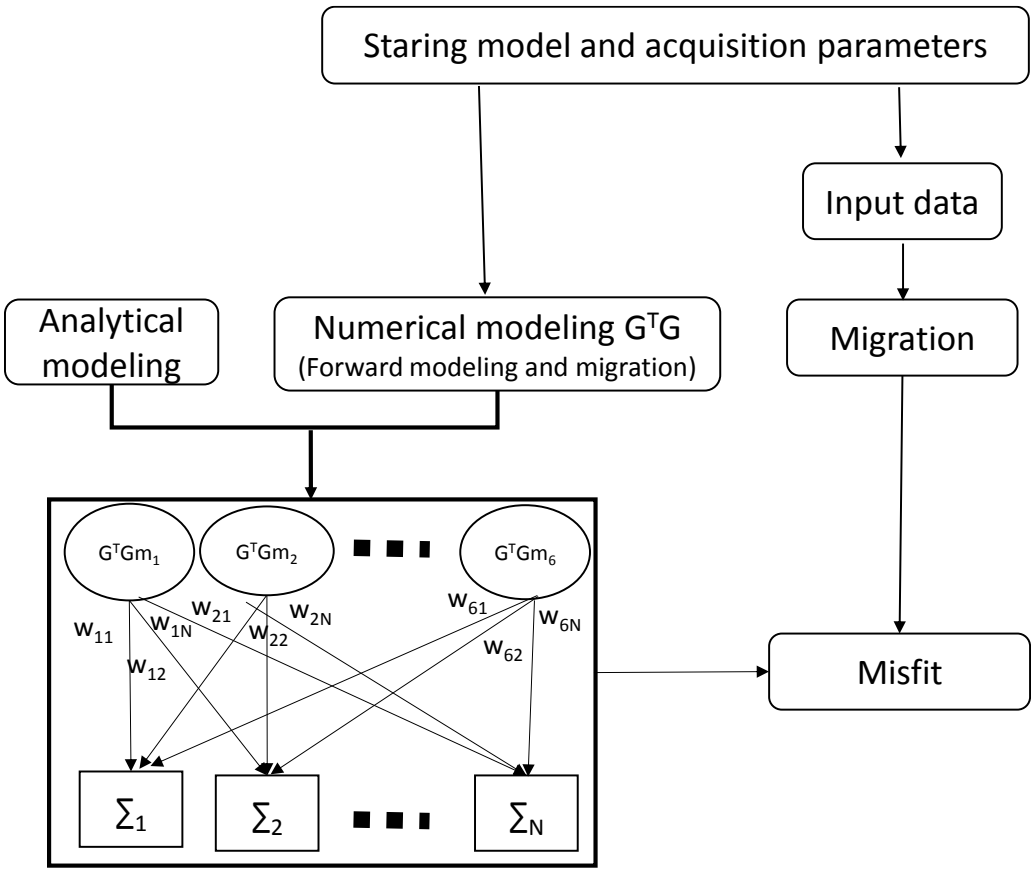

Figure 8: Flow work for AVO/Az analysis using basis dictionaries and constrained solution. The numerical AVO/Az values is modeled and migrated based on the same migration and acquisition parameters as seismic input data. These parameters are not included in analytical AVO/AZ evaluations.

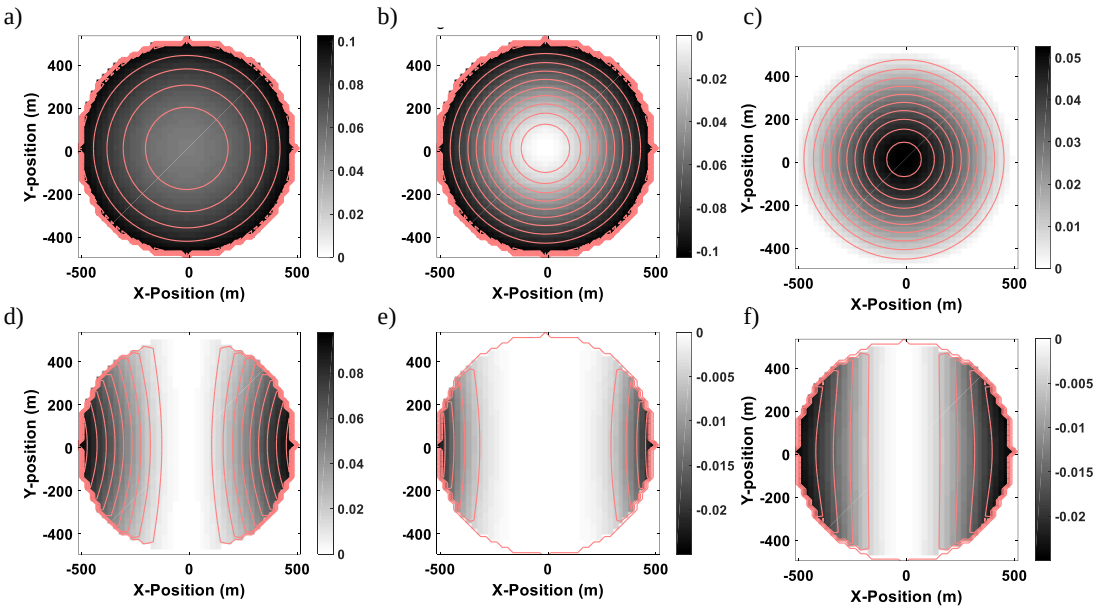

Figure 9: Basis function for the analytical dictionary. The panel in a), b) and c) are the evaluation of isotropic parameters, $\alpha_1 = \alpha_2 = \alpha_3 = 0.1$ respectively. The panel in d), e) and f) are the evaluation of anisotropic parameters, $\alpha_5 = 0.1$, $\alpha_4 = -0.1$ and $\alpha_6 = -0.1$ respectively.

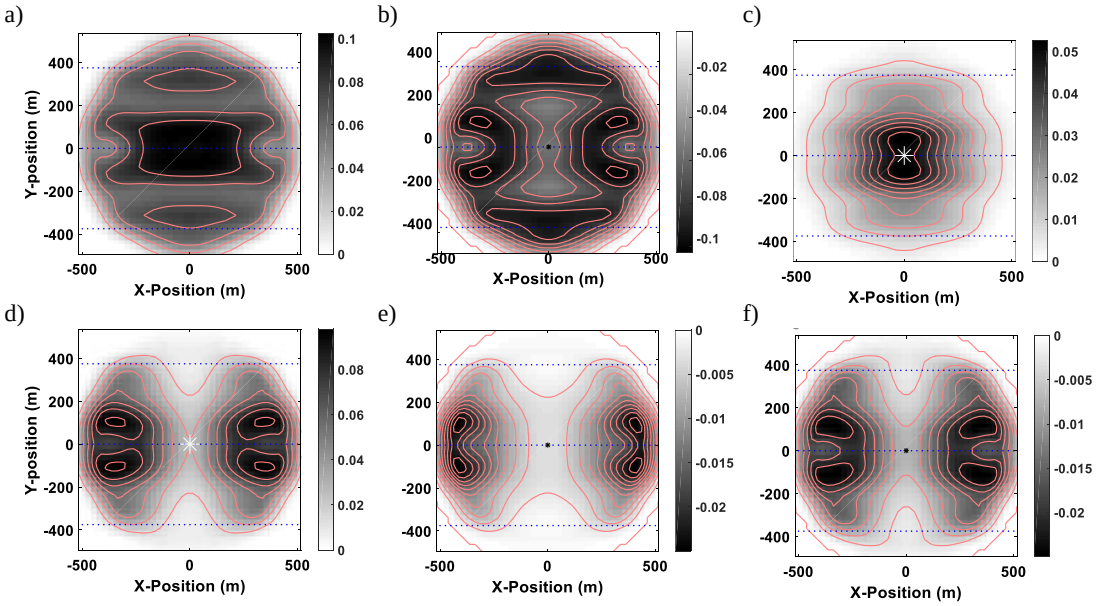

Figure 10: Basis functions for the numerical dictionary including distortion by sampling. The panel in a), b) and c) are the evaluation of isotropic parameters, $\alpha_1 = \alpha_2 = \alpha_3 = 0.1$ respectively. The panel in d), e) and f) are the evaluation of anisotropic parameters, $\alpha_5 = 0.1$, $\alpha_4 = -0.1$ and $\alpha_6 = -0.1$ respectively. The dotted lines in represent three receiver lines with $dx_{rec} = 25$ and $dy_{rec} = 375$ m and the star sign "*" in middle of figures are the position of the scatter point.

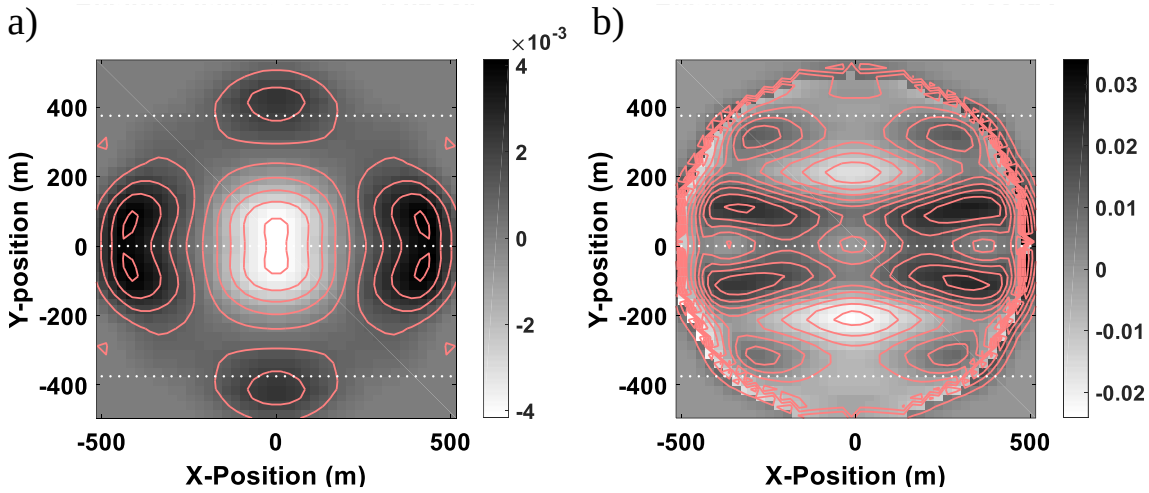

Figure 11: The residual norm of migration of true data and sum of optimal weights multiplied by basis dictionaries obtained from a) numerical evaluation and b) the corresponding values in analytical evaluations.

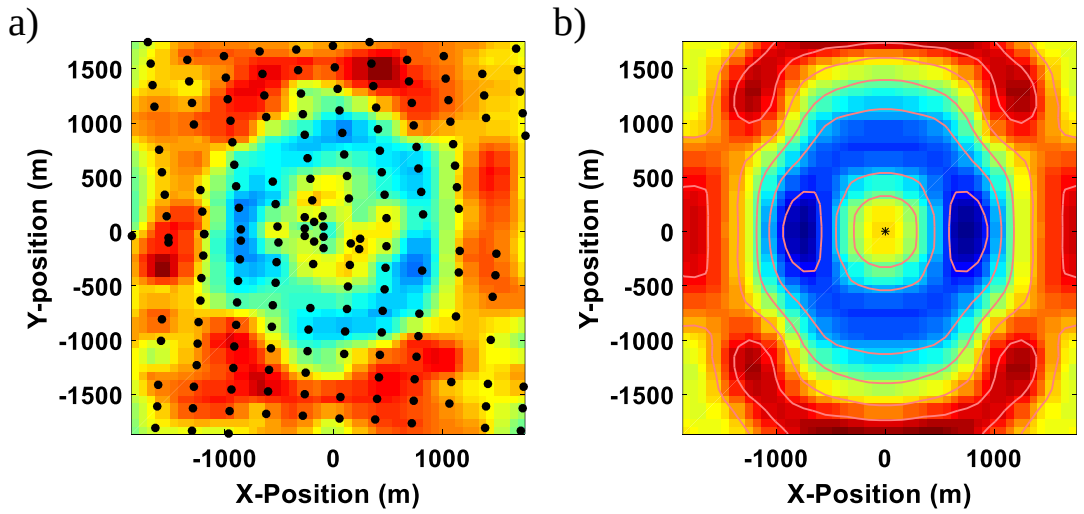

Figure 12: AVO/Az least squares fitting of true data shown in (a) is compared to resultant dictionaries obtained from numerical evaluation as shown in (b). The dots in (a) represents the position of the sources.

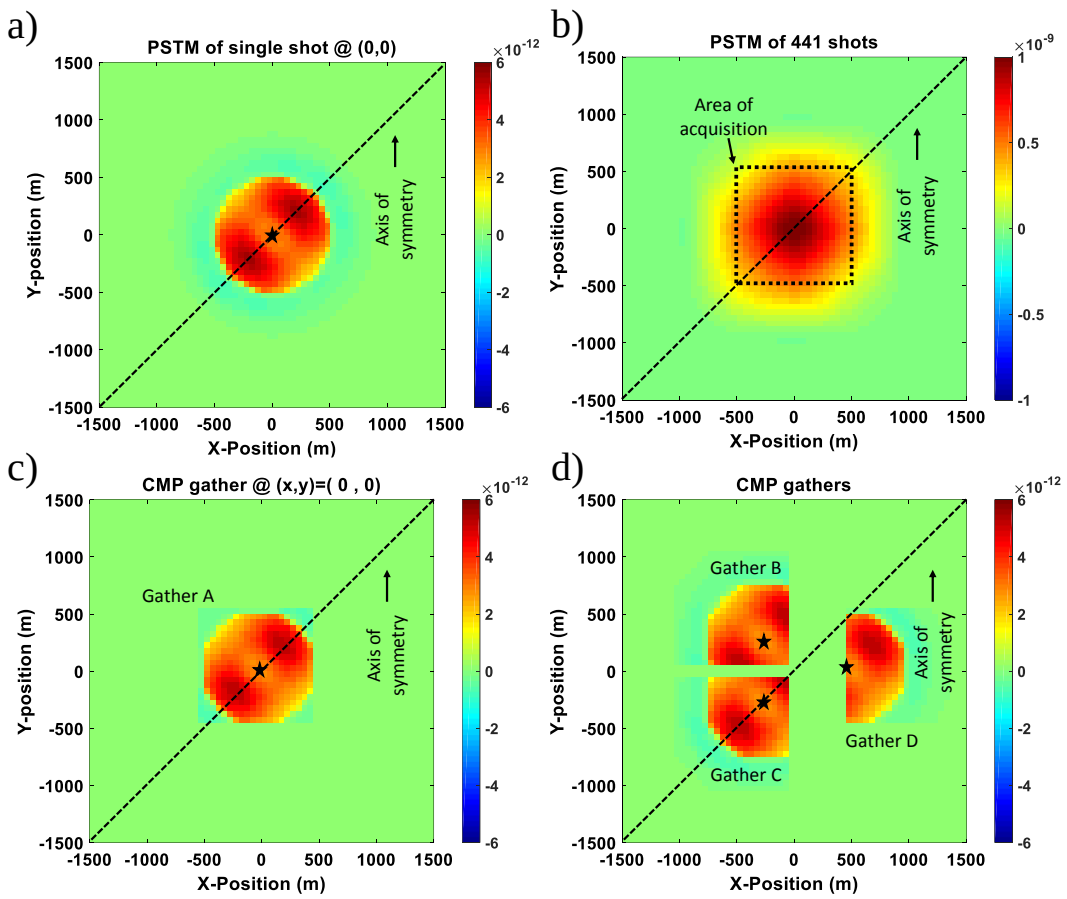

Figure 13: Multi-shot PSTM gather. a) The PSTM of single shot record at (x, y)=(0,0) m in the model. b) PSTM of 441 shot records acquired within the dotted box. c) The PSTM gather A formed from the at (x , y)=(0,0) m in the model. d) The PSTM gather at A, B, C which are overlain on their position.